Supporting Information

69451 Weinheim, Germany

Abstract: Aluminium batteries constitute a safe and sustainable high energy-density electrochemical energy storage solution. Viable rechargeable batteries require suitable electrode materials that can readily intercalate high-charge Al^{3+} ions. Here, we investigate the Al^{3+} intercalation chemistry of anatase TiO_2 and uncover how chemical modifications control the structural accommodation of the Al^{3+} ions. We use fluoride- and hydroxide doping to generate high concentrations of titanium vacancies. The co-existence and interplay of hetero-anions and vacancies lead to a complex insertion mechanism implying three distinct types of host sites, the native interstitials sites, the single and paired vacant sites. We demonstrate that Al^{3+} induces a strong local distortion, which affects the insertion properties of the neighboured host sites. Overall, specific structural features induced by the intercalation of Al^{3+}, should be considered when designing new electrode materials for multi-valent batteries.

DOI: 10.1002/anie.2016XXXXX

Table of Contents

Experimental Procedures

Synthesis

The defective hydroxyfluorinated anatase ($Ti_{0.78}\square_{0.22}O_{1.12}F_{0.40}(OH)_{0.48}$) was synthesized using a solution-based solvothermal synthesis described in our previous report.[1] Briefly, a solution containing 1.2 mL of HF and 24.8 mL of isopropanol was added to 4 mL of titanium isopropoxide in a 45 mL Teflon line container with a fixed ratio of F/Ti setting at 2. After sealing, the solution was heated at 90 °C for 12 hours. The white precipitate was separated from the solution using centrifugation and washed several times with ethanol. The recovered powder was dried at 80 °C overnight, and further outgassed at 150 °C overnight under vacuum. (Caution: HF is a highly corrosive acid and proper protective equipment is mandatory.) The chemical formula was determined as follow: ^{19}F NMR was used to determine the fluorine content, the vacancy concentration was quantified by structural analysis of the PDF data and the OH content was deduced from charge neutrality.

Electrochemical and Synchrotron X-ray Scattering and STEM characterizations

The working electrode was composed of 80 wt% $Ti_{0.78}\square_{0.22}O_{1.12}F_{0.4}(OH)_{0.48}$ active material, 10 wt% conductive carbon (Super P, Timcal), and 10 wt% polytetrafluoroethylene (PTFE, 60 wt % dispersion in water, Aldrich) binder, and coated on a glassy carbon plate (HTW Germany) at the geometrical active mass density of 2 mg cm^{-2}. Al wire and Al metal plate were used as the reference electrode and the counter electrode, respectively. A chloroaluminate based ionic liquid (1-ethyl-3-methylimidazolium chloride ([EMIm]Cl)-$AlCl_3$ mixture, molar ratio 1:1.1) was used as the electrolyte. [EMIm]Cl (98%, Sigma-Aldrich) was dried at 120 °C under vacuum (< 1 Pa) for 12 h, then anhydrous $AlCl_3$ (99.99%, ultra-dry, Alfa Aesar) was slowly added under stirring condition with a fixed mole ratio of 1:1.1 in an argon-filled glove box. Borosilicate glass-fiber filter paper (Whatmann grade GF/D) was used as the separator. Three-electrode Swagelok-type cells were assembled in an argon-filled glove box. Electrochemical measurements were performed in the potential range of 0.01-1.8 V vs. Al^{3+}/Al with a Biologic MPG-2 system at 25 °C. The cells were cycled under 20 mA g^{-1} corresponding to 5-6 hours of charge-discharge duration. To obtain an insight picture of Al insertion/extraction process during the electrochemical reaction, Swagelok cells with active electrode materials at the end of discharge and end of charge were disassembled in the glove box and electrodes were washed with tetrahydronfuran (THF). After evacuating the THF, the active materials were scraped off from glassy carbon plates, loaded inside in Kapton capillaries and sealed in the Argon-filled glove box to avoid exposing to air. High energy synchrotron X-ray (λ = 0.2128 Å) scattering characterization were collected at the 11-ID-B beamline at the Advanced Photon Source at Argonne National Laboratory. One-dimensional diffraction data were obtained by integrating the raw 2D total scattering data in Fit2D.[2] PDFs were extracted from the background and Compton scattering corrected data following Fourier transformation using PDFgetX2.[3] The PDFs were subsequently modelled using PDFgui software.[4]
The electrode material was dispersed in ethanol, transferred to TEM copper grid by droplet casting and then dried on a plate oven at ~60 °C for several minutes. An FEI Titan 80-200 ChemiSTEM microscope equipped with Super-X energy-dispersive X-ray (EDX) spectroscopy was used to characterize the chemical composition of the electrode materials at 200 kV.

Solid state NMR

The aluminized sample was stored before and between NMR experiments in a glove box under dry nitrogen gas. NMR rotors were filled inside the glove box and, after being inserted manually into the magnet, they were spun under dry nitrogen atmosphere during the course of the NMR experiment.
^{19}F MAS NMR. ^{19}F (I = 1/2) MAS NMR spectra of the aluminized sample were recorded at RT, using a Hahn echo sequence with an interpulse delay equal to one rotor period, on a Bruker Avance III WB 300 MHz (7.0 T, ^{19}F Larmor frequency of 282.4 MHz) and a Bruker Avance III WB 850 MHz (20.0 T, ^{19}F Larmor frequency of 800.1 MHz). ^{19}F MAS NMR spectra were acquired on the 300 MHz spectrometer using a 1.3 mm ultrafast MAS probe. 90° pulse lengths were 1.65 µs (corresponding to a nutation frequency 152 kHz) and 128 transients were accumulated with recycle delays of 10 s. ^{19}F MAS NMR spectra were also recorded on the 850 MHz spectrometer using a 1.3 mm MAS probe. 90° pulse durations were 1 µs (corresponding to a nutation frequency of 250 kHz) and 64 transients were accumulated with recycle delays of 10 s. The ^{19}F MAS NMR spectrum of $Ti_{0.78}\square_{0.22}O_{1.12}F_{0.4}(OH)_{0.48}$ was acquired on a 300 MHz spectrometer as described in our previous report.[1] All ^{19}F spectra are referenced to $CFCl_3$.
^{19}F-^{27}Al double-resonance MAS NMR experiments were carried out at 20.0 T with a spinning frequency of 60 kHz on the aluminized $Ti_{0.78}\square_{0.22}O_{1.12}F_{0.40}(OH)_{0.48}$ sample 163 days after the preparation. The experiment is based on the phase-modulated rotational-echo saturation-pulse (PM-RESPDOR) scheme[5] where dipolar recoupling pulses are omitted, such that the dephasing of the ^{19}F signal is driven by ^{27}Al-^{19}F indirect (J) spin-spin couplings and/or residual dipolar splittings due to higher-order cross terms.[6] It consists of a ^{19}F rotor-synchronized Hahn echo experiment with and without applying a ^{27}Al phase-modulated (PM) saturation pulse in the middle of the echo period for the dephased and reference spectra, respectively. The difference between the dephased and reference spectra highlights the ^{19}F resonances of the ^{19}F nuclei coupled (i.e. in the vicinity) to ^{27}Alnuclei. The half-echo dephasing time was set to 917 µs (55 rotor periods) and the duration of the PM-saturation pulse (167 µs, i.e. 10 rotor periods) was taken into account for the reference experiment. 64 scans with a recycle delay of 10 s were accumulated for the dephased and reference spectra.
^{27}Al MAS NMR. ^{27}Al (I = 5/2) MAS spectra were acquired at RT on a Bruker Avance III WB 850 MHz (20.0 T, ^{27}Al Larmor frequency of 221.5 MHz) using a 1.3 mm ultrafast MAS probe. Quantitative ^{27}Al one-dimensional (1D) MAS spectra were recorded with an excitation pulse length of 0.5 µs, i. e., a flip angle of π/12 (radio-frequency field ν_{RF} = 83.3 kHz).[7] 1024 up to 8096 transients were recorded with a recycle delay of 0.5 s.
The two-dimensional (2D) z-filtered ^{27}Al multiple-quantum magic angle spinning (MQMAS) experiments[8,9] were performed on the aluminized $Ti_{0.78}\square_{0.22}O_{1.12}F_{0.40}(OH)_{0.48}$ sample 46 days after the preparation using a spinning frequency of 64 kHz, with triple quantum (3Q) excitation and reconversion pulse lengths of 1.6 and 0.6 µs, respectively (ν_{RF} ~ 270 kHz). The z-filter duration was 29.4 µs (one rotor period) and the 90° central transition selective pulse duration was 6.5 µs (ν_{RF} = 12.8 Hz). Acquisition in the indirect dimension was rotor-synchronized[10] and 14 t_1 increments of 31.2 µs with XX transient each were collected with a recycle delay of 0.5 s. All ^{27}Al spectra are referenced with respect to a 1 M solution of $Al(NO_3)_3$.
NMR spectra were simulated using the DMFit software.[11]

Density Functional Theory calculations

All density functional theory (DFT) calculations were performed using the code VASP[12,13], with valence electrons described by a plane-wave basis with a cut-off of 500 eV. Interactions between core and valence electrons were described using the projector augmented wave (PAW) method[14], with cores of [Mg] for Ti, [He] for O, [He] for F, [Ne] for Al, and [H^+] for H. The calculations used the revised Perdew-Burke-Ernzerhof generalized gradient approximation function PBEsol[15], with a Dudarev +U correction applied to the Ti d states (GGA+U)[16,17]. We use a $U_{Ti,d}$ value of 4.2 eV, which has previously been used to model intercalation of lithium and other metal ions in anatase TiO_2 and TiO_2(B)[18–21]. To model anatase TiO_2, we first performed a full geometry optimisation on a single Ti_4O_8 unit cell, with optimised lattice parameters obtained by fitting a series of constant-volume calculations to the Murnaghan equation of state. All subsequent calculations were

fixed to the resulting optimised lattice parameters. Intercalation into stoichiometric anatase TiO_2 was modelled using a 4 × 4 × 2 supercell (384 atoms), with a single Al ion inserted at the interstitial site ($AlTi_{128}O_{256}$). To model intercalation at single- and double-titanium vacancies, we performed a series of calculations in 4 × 4 × 2 supercells, with either 1 Ti vacancy plus 4 charge-compensating F or OH anions, giving a cell stoichiometries of $Ti_{127}O_{252}X_4$ (X=F, OH), or 2 Ti vacancies plus 8 charge-compensating F anions, giving a cell stoichiometry of $Ti_{126}O_{248}F_8$. In both cases, we consider models in which fluoride ions occupy anion sites adjacent to the Ti vacancies, which we have previously shown minimized the DFT-calculated energy[1,22,23]. Individual calculations were deemed optimised when all atomic forces were smaller than 0.01 eV $Å^{-1}$. All calculations were spin-polarized, and included Γ only when sampling ***k***-space. To calculate intercalation energies, a reference calculation for metallic Al was performed using the same convergence criteria as above. For this reference calculation, we considered a 2-atom cell, and used a 16 × 16 × 16 Monkhorst-Pack grid for ***k***-space sampling.

A dataset containing all DFT calculation inputs and outputs is available at the University of Bath Research Data Archive, published under the CC-BY-4.0 license[24]. This dataset also contains analysis scripts used to post-process the DFT data and to generate Fig. 5 and Fig. S11. The data analysis scripts use the Python packages numpy[25,26], pymatgen[27], snakemake[28], and vasppy[29].

Results and Discussion

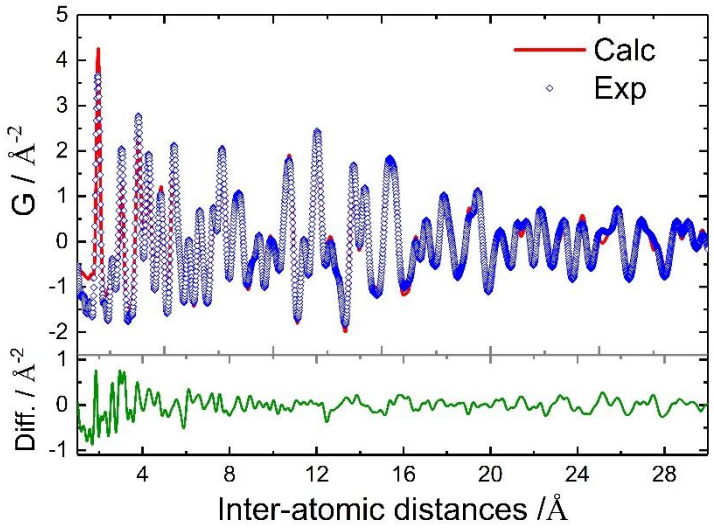

Figure S1. PDF refinement of the discharged electrode (R_w = 22.2 %).

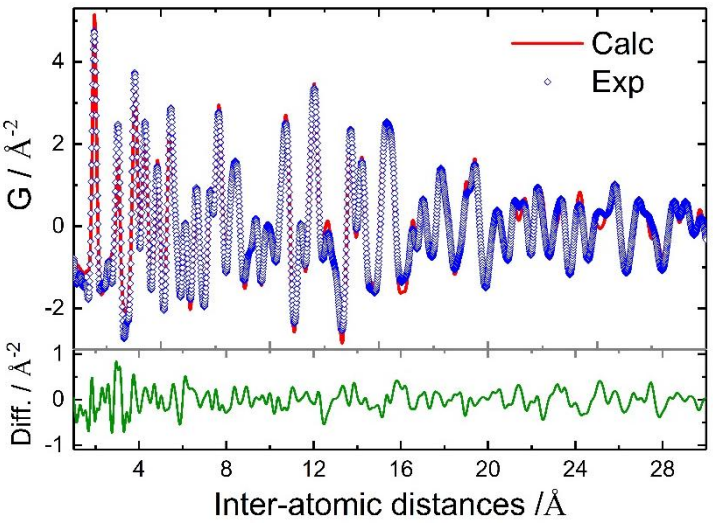

Figure S2. PDF refinement of the charged electrode (R_w = 18.8 %).

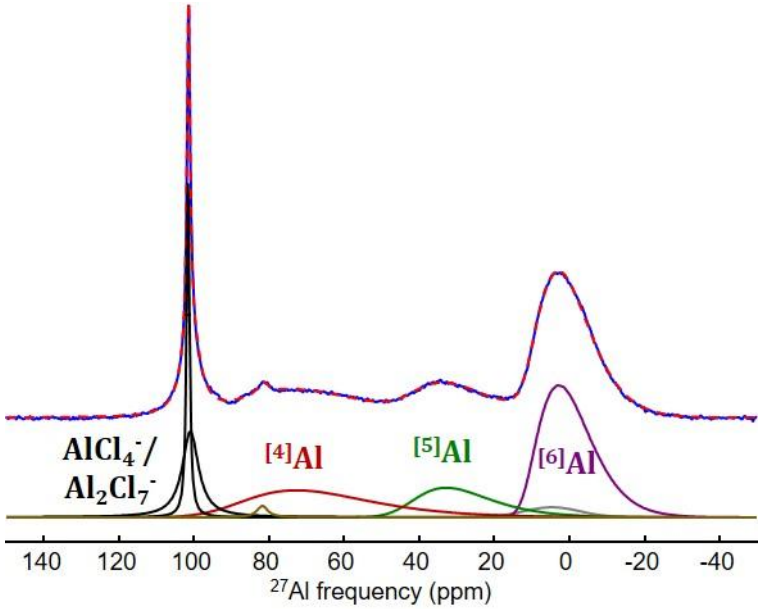

Figure S3. Experimental (blue) and fitted (red dashed) one-dimensional ^{27}Al MAS (64 kHz) NMR (20 T) spectra of the central transitions of the discharged $Ti_{0.78}\square_{0.22}O_{1.12}F_{0.40}(OH)_{0.48}$ sample 15 days after the preparation. The individual contributions used for the fit (see **Table S1**) are shown below and the assignments of the main resonances are indicated. The brownish-yellowish line refers to $Al(OH)_4$. The grey line refers to the center band of the $^{[6]}$Al satellite transition pattern.

Table S1. Average isotropic chemical shift ($<\delta_{iso}>$), full width at half maximum (FWHM) of the isotropic chemical shift Gaussian distribution (ΔCS), average quadrupolar frequency ($<\nu_Q>$) and quadrupolar constant ($<C_Q>$), FWHM of the statistical quadrupolar frequency distribution ($\Delta\nu_Q$) along V_{ZZ} used to simulate the contributions assigned to the $^{[n]}$Al sites in anatase of the discharged $Ti_{0.78}\square_{0.22}O_{1.12}F_{0.40}(OH)_{0.48}$ sample 15 days after the preparation. Isotropic chemical shifts (δ_{iso}) and fwhm of the Lorentzian lines used to simulate the contributions of impurities. Relative intensities of these NMR lines for the sample (I) and relative intensities of the $^{[n]}$Al sites in anatase (*I'*). In bold, sum of the relative intensities of the NMR lines assigned to the $^{[n]}$Al sites in anatase and to $AlCl_4^-/Al_2Cl_7^-$ in the sample.

$<\delta_{iso}>$ (ppm)	ΔCS (ppm)	$<\nu_Q>$ (kHz)	$<C_Q>$ (MHz)	$\Delta\nu_Q$ (kHz)	I (%)	*I' (%)*	Assignment
11.2	6.2	1400	9.33	560	42.5	*55.0*	$^{[6]}$Al
43.7	12.2	1600	10.67	800	13.9	*18.0*	$^{[5]}$Al
91.0	20.0	2060	13.73	1000	20.8	*26.9*	$^{[4]}$Al
					77.2		
δ_{iso} (ppm)	FWHM (ppm)						
101.4	1.0				9.1		$AlCl_4^-/Al_2Cl_7^-$
100.8	5.3				12.5		$AlCl_4^-/Al_2Cl_7^-$
					21.6		
81.6	3.5				1.1		$Al(OH)_4^-$

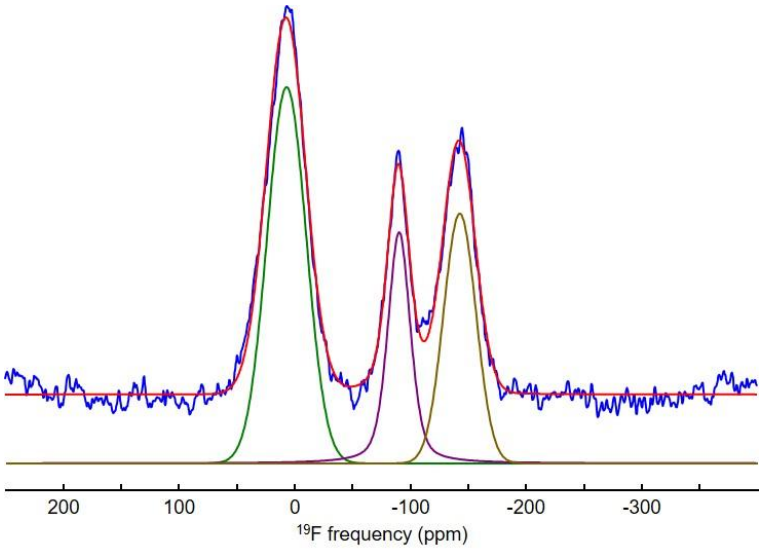

Figure S4. Experimental (blue) and fitted (in red) ^{19}F MAS (64 kHz) NMR (7.0 T) spectra of the aluminized $Ti_{0.78}\square_{0.22}O_{1.12}F_{0.40}(OH)_{0.48}$ sample 32 days after the preparation. The individual resonances used for the fit are shown below (see **Table S2**).

Table S2. Isotropic chemical shifts δ_{iso}, full-width at half-maximum (fwhm), and relative intensities I of the NMR lines obtained from the reconstruction of the ^{19}F MAS (64 kHz) NMR spectrum of the aluminized $Ti_{0.78}\square_{0.22}O_{1.12}F_{0.40}(OH)_{0.48}$ sample 32 days after the preparation and tentative assignment of these NMR lines.

δ_{iso} (ppm)	fwhm (ppm)	I (%)	Assignment
7.3	39.7	50.9	$Ti^{IV}_2\square$-F
-89.9	22.8	21.0	Ti^{IV}_3-F, $Ti^{IV}Ti^{III}\square$-F
-142.3	33.0	28.1	$Ti^{III}_2\square$-F, $Ti^{IV}_2Ti^{III}$-F, Ti^{IV}_2Al-F, Ti^{IV}Al$\square$-F, Ti^{III}Al$\square$-F

Discussion about the tentative assignments of the ^{19}F NMR resonances

The intercalation of one Al^{3+} ion being balanced by the reduction of three Ti^{4+} ions into Ti^{3+} ions, the number of potential fluorine environments dramatically increases from the pristine compound to the aluminized samples:

- $Ti^{IV}\square_2$-F can be converted into $Ti^{III}\square_2$-F, $Ti^{IV}Al\square$-F, $Ti^{IV}Al_2$-F, $Ti^{III}Al\square$-F and $Ti^{III}Al_2$-F;
- $Ti^{IV}_2\square$-F can be converted into $Ti^{IV}Ti^{III}\square$-F, $Ti^{III}_2\square$-F, Ti^{IV}_2Al-F, $Ti^{IV}Ti^{III}Al$-F and Ti^{III}_2Al-F;
- Ti^{IV}_3-F can be converted into $Ti^{IV}_2Ti^{III}$-F, $Ti^{IV}Ti^{III}_2$-F and Ti^{III}_3-F.

Nevertheless, keeping in mind that, in the pristine compound, fluoride ions are preferentially located close to vacancies,[1] i.e., are reluctant to be threefold coordinated, that the aluminized samples remain defective, and that in TiF_3[30] and in the various phases of AlF_3,[31–33] fluoride ions are two-fold coordinated, three-fold coordinated fluorine environments such as Ti^{IV}_2Al-F, $Ti^{IV}Ti^{III}Al$-F, Ti^{III}_2Al-F, $Ti^{IV}Al_2$-F, $Ti^{III}Al_2$-F, $Ti^{IV}Ti^{III}_2$-F, Ti^{III}_3-F are unlikely to occur.

Based on the ^{19}F NMR chemical shift values of the environments $Ti^{IV}\square_2$-F (98 ppm), $Ti^{IV}_2\square$-F (-4 ppm) and Ti^{IV}_3-F (-88 ppm) in $Ti_{0.78}\square_{0.22}O_{1.12}F_{0.40}(OH)_{0.48}$,[1] Al_2-F (~ - 172 ppm) in the various AlF_3 phases[34] and Ti^{III}_2-F (-145 ppm) in TiF_3[18] and on the decrease of the ^{19}F chemical shift value when the coordination number of fluorine increases, the intercalation of Al^{3+} ion in a titanium vacancy and the reduction of a Ti^{4+} ion into a Ti^{3+} ion are both expected to induce a decrease of the δ_{iso} value of the neighbouring ^{19}F nucleus. A decrease (an increase) of the relative intensities of the NMR resonances of higher (smaller) chemical shift, the vanishing of the NMR line assigned to $Ti^{IV}\square_2$-F and the occurrence of a broad NMR line at lower chemical shift are indeed observed when Al^{3+} ions are inserted. The expected evolution of the ^{19}F δ_{iso} values of the F environments in the aluminized sample compared to the ^{19}F δ_{iso} values of the F environments in $Ti_{0.78}\square_{0.22}O_{1.12}F_{0.40}(OH)_{0.48}$ and to the ^{19}F δ_{iso} values of the NMR resonances in the aluminized sample (**Figure S4**, **Table S2**), led us to tentatively assign the ^{19}F NMR resonances to some of the potential species of the aluminized sample (**Figure S5**). The ^{19}F δ_{iso} values of the species Ti^{III}_3-F, $Ti^{IV}Ti^{III}_2$-F, $Ti^{IV}Ti^{III}Al$-F, Ti^{III}_2Al-F, $Ti^{IV}Al_2$-F and $Ti^{III}Al_2$-F are assumed to be lower than the lowest observed ^{19}F δ_{iso} value. As expected, these species would therefore do not occur in the aluminized sample.

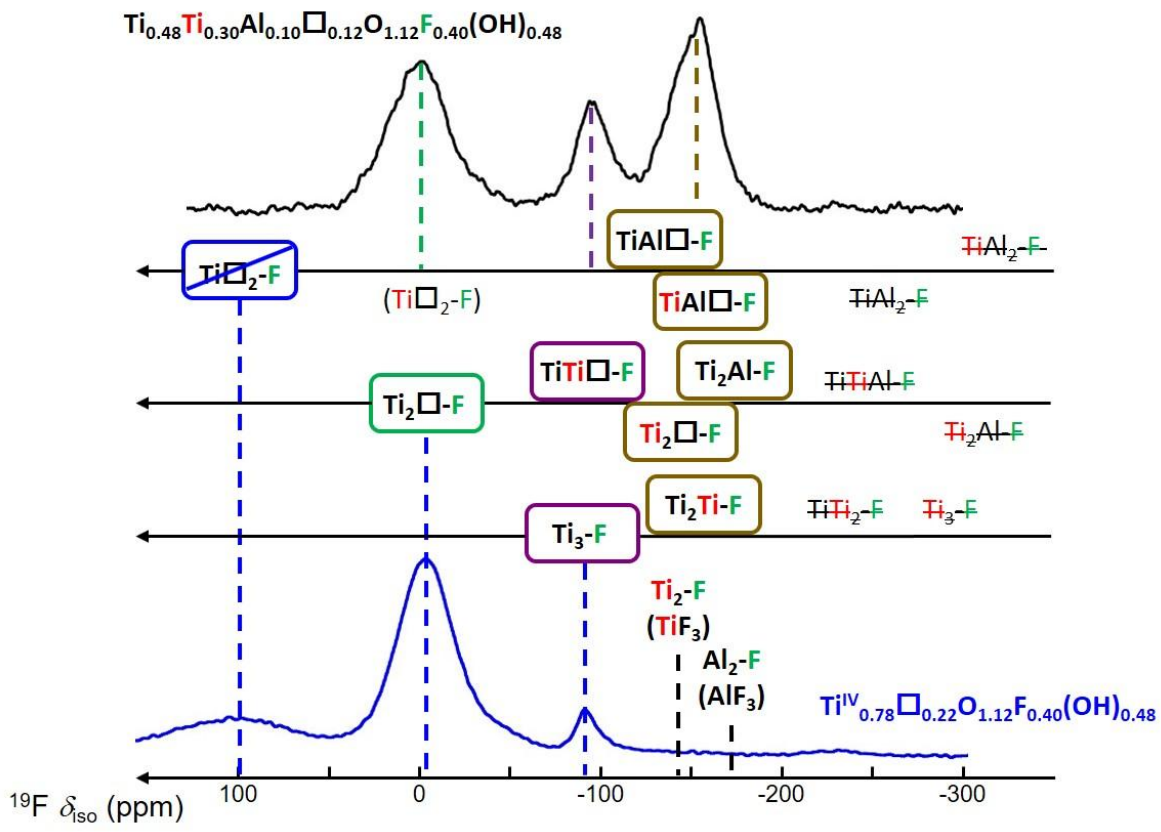

Figure S5. Schematic illustration of the expected evolution of the ^{19}F δ_{iso} values of the F environments in the aluminized sample (framed in green, mauve and brown) compared to the ^{19}F δ_{iso} values of the F environments in $Ti_{0.78}\square_{0.22}O_{1.12}F_{0.40}(OH)_{0.48}$ (dashed blue), in TiF_3 and in AlF_3 (dashed black), and assignment of the F environments in the aluminized sample to the ^{19}F NMR resonances (dashed green, mauve and brown). Ti^{IV} in black and Ti^{III} in red.

Time-dependent NMR study

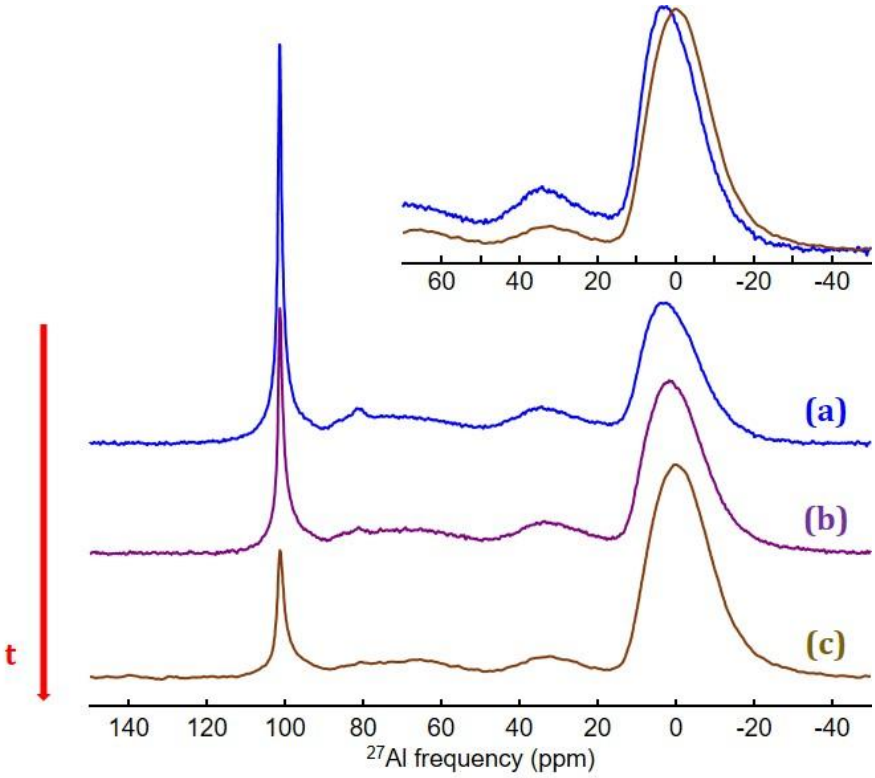

Figure S6. One-dimensional ^{27}Al MAS ((a) and (b): 64 kHz, (c): 60 kHz) NMR (20 T) spectra of the central transitions of aluminized $Ti_{0.78}\square_{0.22}O_{1.12}F_{0.40}(OH)_{0.48}$ sample recorded at different time points (t refers to time) relative to the preparation: (a) 15 days, (b) 46 days, (c) 175 days. Inset: $^{[6]}$Al contributions of (a) and (c). The sample was stored in a glove box in between the different experiments.

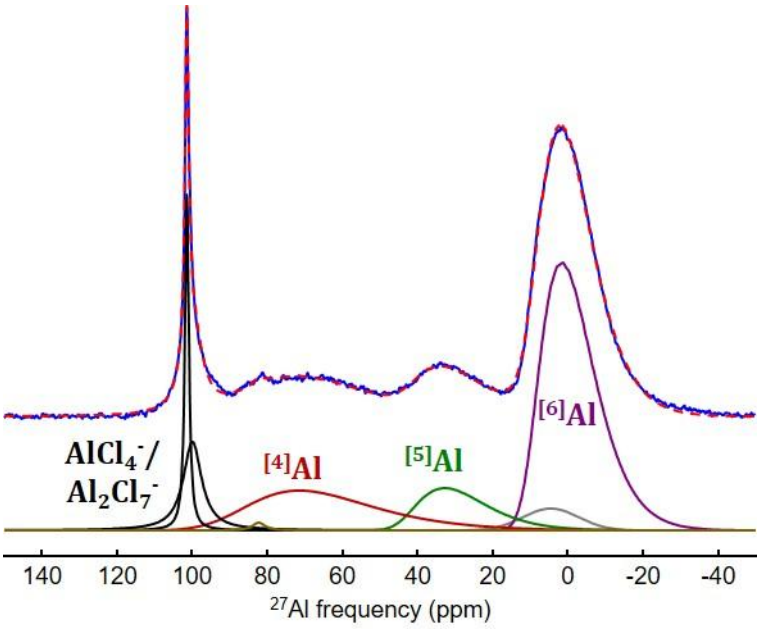

Figure S7. Experimental (blue) and fitted (red dashed) one-dimensional ^{27}Al MAS (64 kHz) NMR (20 T) spectra of the central transitions of the aluminized $Ti_{0.78}\square_{0.22}O_{1.12}F_{0.40}(OH)_{0.48}$ sample 46 days after the preparation. The individual contributions used for the fit (see **Table S3**) are shown below and the assignments of the main resonances are indicated. The grey line refers to the center band of the $^{[6]}$Al satellite transition pattern.

Table S3. Average isotropic chemical shift ($<\delta_{iso}>$), full width at half maximum (FWHM) of the isotropic chemical shift Gaussian distribution (ΔCS), average quadrupolar frequency ($<\nu_Q>$) and quadrupolar constant ($<C_Q>$), FWHM of the statistical quadrupolar frequency distribution ($\Delta\nu_Q$) along V_{ZZ} used to simulate the contributions assigned to the $^{[n]}$Al sites in anatase of the aluminized $Ti_{0.78}\square_{0.22}O_{1.12}F_{0.40}(OH)_{0.48}$ sample 46 days after the preparation. Isotropic chemical shifts (δ_{iso}) and fwhm of the Lorentzian lines used to simulate the contributions of impurities. Relative intensities of these NMR lines for the sample (I) and relative intensities of the $^{[n]}$Al sites in anatase (*I'*) assuming that the hydrolysis of the chloroaluminate species only produces $^{[6]}$Al sites. In bold, sum of the relative intensities of the NMR lines assigned to $AlCl_4^-/Al_2Cl_7^-$ in the sample.

$<\delta_{iso}>$ (ppm)	ΔCS (ppm)	$<\nu_Q>$ (kHz)	$<C_Q>$ (MHz)	$\Delta\nu_Q$ (kHz)	I (%)	*I' (%)*	Assignment
10.2	7.3	1400	9.33	600	54.3	*62.2*	$^{[6]}$Al
43.4	9.2	1580	10.53	700	10.9	*14.1*	$^{[5]}$Al
90.0	20.0	2060	13.73	990	18.4	*23.8*	$^{[4]}$Al
δ_{iso} (ppm)	fwhm (ppm)						
101.4	1.2				7.1		$AlCl_4^-/Al_2Cl_7^-$
99.9	5.9				8.8		$AlCl_4^-/Al_2Cl_7^-$
					15.9		
82.2	4.0				0.5		$Al(OH)_4^-$

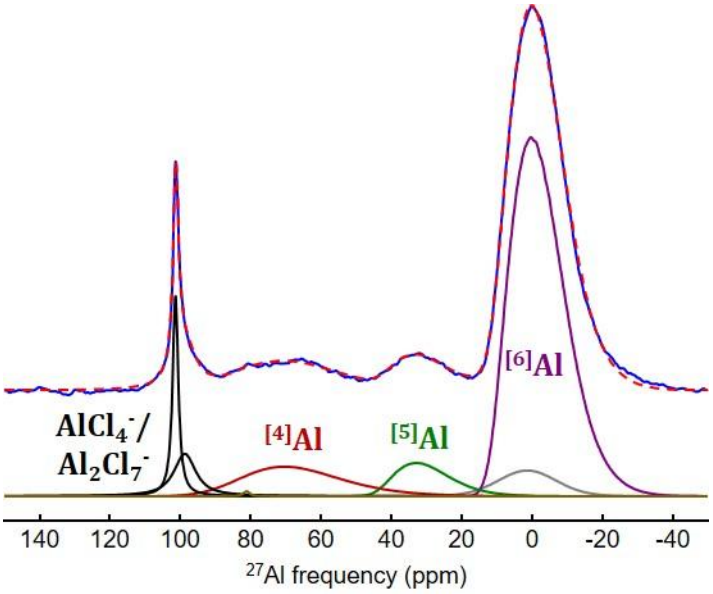

Figure S8. Experimental (blue) and fitted (red dashed) one-dimensional 1D ^{27}Al MAS (64 kHz) NMR (20 T) spectra of the central transitions of the aluminized $Ti_{0.78}\square_{0.22}O_{1.12}F_{0.40}(OH)_{0.48}$ sample 175 days after the preparation. The individual contributions used for the fit (see **Table S4**) are shown below and the assignments of the main resonances are indicated. The grey line correspond to the center band of the $^{[6]}$Al satellite transition pattern.

Table S4. Average isotropic chemical shift ($<\delta_{iso}>$), full width at half maximum (FWHM) of the isotropic chemical shift Gaussian distribution (ΔCS), average quadrupolar frequency ($<\nu_Q>$) and quadrupolar constant ($<C_Q>$), FWHM of the statistical quadrupolar frequency distribution ($\Delta\nu_Q$) along V_{ZZ} used to simulate the contributions assigned to the $^{[n]}$Al sites in anatase of the aluminized $Ti_{0.78}\square_{0.22}O_{1.12}F_{0.40}(OH)_{0.48}$ sample 175 days after the preparation. Isotropic chemical shifts (δ_{iso}) and fwhm of the Lorentzian lines used to simulate the contributions of impurities. Relative intensities of these NMR lines for the sample (I) and relative intensities of the $^{[n]}$Al sites in anatase (*I'*) assuming that the hydrolysis of the chloroaluminate species only produces $^{[6]}$Al sites. In bold, sum of the relative intensities of the NMR lines assigned to the $^{[n]}$Al sites in anatase and to $AlCl_4^-/Al_2Cl_7^-$ in the sample.

$<\delta_{iso}>$ (ppm)	ΔCS (ppm)	$<\nu_Q>$ (kHz)	$<C_Q>$ (MHz)	$\Delta\nu_Q$ (kHz)	I (%)	*I' (%)*	Assignment
10.5	6.7	1480	9.87	465	71.8	*77.7*	$^{[6]}$Al
42.8	7.5	1470	9.80	530	6.7	*8.6*	$^{[5]}$Al
86.3	20.0	1820	12.13	760	10.6	*13.7*	$^{[4]}$Al
δ_{iso} (ppm)	fwhm (ppm)						
101.3	1.9				6.1		$AlCl_4^-/Al_2Cl_7^-$
98.6	7.4				4.8		$AlCl_4^-/Al_2Cl_7^-$
					10.9		
81.1	2.1				0.1		$Al(OH)_4^-$

Table S5. Relative intensities (%) of the ^{27}Al NMR resonances of the $^{[6]}$Al, $^{[5]}$Al and $^{[4]}$Al sites and of the chloro and hydroxy aluminate species in the aluminized sample and, between parentheses, proportion of $^{[6]}$Al, $^{[5]}$Al and $^{[4]}$Al sites in anatase (assuming that the hydrolysis of the chloroaluminate species only produces $^{[6]}$Al sites).

t (days)	$^{[6]}$Al	$^{[5]}$Al	$^{[4]}$Al	$AlCl_4^-$, $Al_2Cl_7^-$	$Al(OH)_4^-$
15	42.5 (55.0)	13.9 (18.0)	20.8 (27.0)	21.6	1.1
46	54.3 (62.2)	10.9 (14.1)	18.4 (23.8)	15.9	0.5
175	71.8 (77.7)	6.7 (8.6)	10.6 (13.7)	10.9	0.1

The partial hydrolysis of the chloroaluminate species probably explains the decrease over time of the relative intensities of their resonances (from ~22% to ~11%, **Table S5 and Figure S6**). Nevertheless, this only accounts for a part of the striking increase over time of the relative intensity (from 42% to 72%) of the resonance assigned to $^{[6]}$Al sites, i.e. the increase of the proportion of $^{[6]}$Al sites (from 55% to 78%) in anatase (**Table S5**). Concomitantly, a shift toward lower δ_{iso} values of this resonance is observed (inset of **Figure S6**). This shows that both the number of $^{[6]}$Al sites and their fluorine-coordination degree increase over time. This highlights the mobility of the Al^{3+}, F^- and OH^- ions enabled by vacancies in the anatase structure and possibly enhanced by an increase of the sample temperature during MAS NMR experiments due to frictional heating.

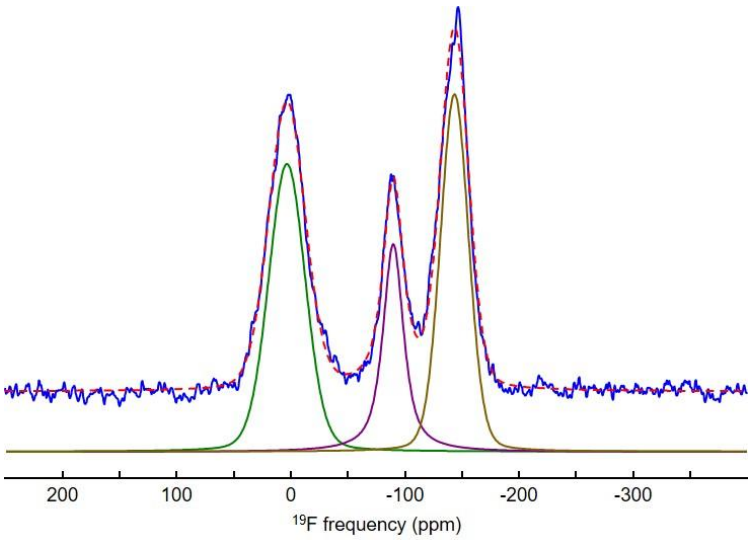

Figure S9. Experimental (blue) and fitted (in red) ^{19}F MAS (64 kHz) NMR (7 T) spectra of the aluminized $Ti_{0.78}\square_{0.22}O_{1.12}F_{0.40}(OH)_{0.48}$ sample 168 days after the preparation. The individual resonances used for the fit are shown below (see **Table S6**).

Table S6. Isotropic chemical shifts δ_{iso}, full width at half maximum (fwhm), and relative intensities I of the NMR lines obtained from the reconstruction of the ^{19}F MAS (64 kHz) NMR spectrum of the aluminized $Ti_{0.78}\square_{0.22}O_{1.12}F_{0.40}(OH)_{0.48}$ sample 168 days after the preparation and tentative assignment of these NMR lines.

δ_{iso} (ppm)	fwhm (ppm)	I (%)	Assignment
3.1	37.8	40.5	$Ti^{IV}_2\square$-F
-90.1	21.3	20.7	Ti^{IV}_3-F, $Ti^{IV}Ti^{III}\square$-F
-143.8	29.1	38.8	$Ti^{III}_2\square$-F, $Ti^{IV}_2Ti^{III}$-F, Ti^{IV}_2Al-F, $Ti^{IV}Al\square$-F, $Ti^{III}Al\square$-F

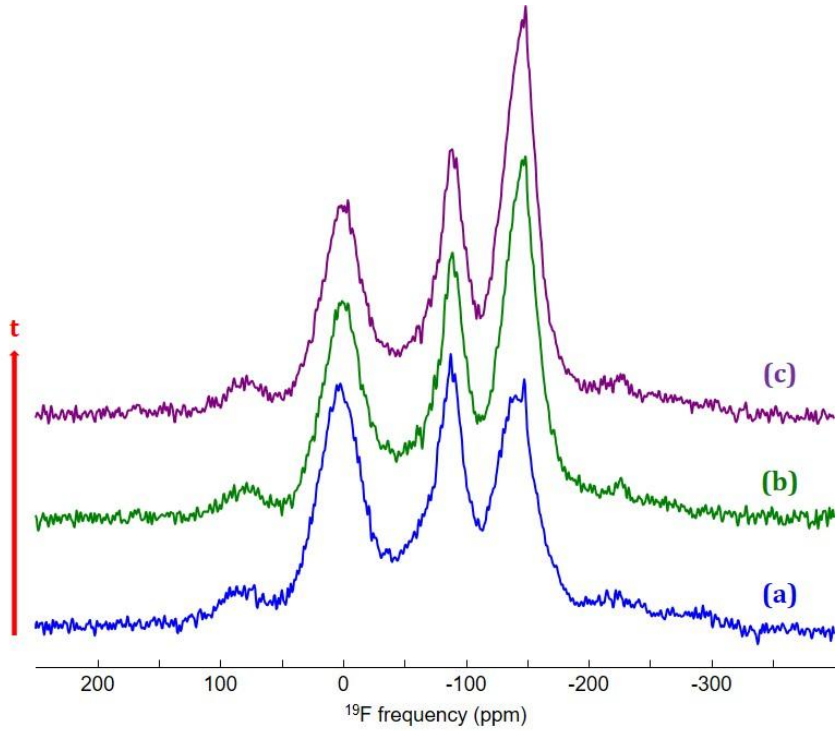

Figure S10. ^{19}F MAS (64 kHz) NMR (20 T) spectra of the aluminized $Ti_{0.78}\square_{0.22}O_{1.12}F_{0.40}(OH)_{0.48}$ sample (a) 15 days (b) 36 days and (c) 168 days after the preparation. t refers to time. The sample was stored in a glove box in between the different experiments.

As observed for ^{27}Al, the relative intensities of the ^{19}F NMR resonances change over time (**Figures S4 and S9, Tables S2 and S6**). These changes can also be observed on the high field spectra (**Figure S10**), even if not quantitative, due to spinning sideband overlaps and possible rotational resonance effects (chemical shift difference between two NMR resonances (~90 ppm) close to MAS frequency (64 kHz = 80 ppm at 20 T for ^{19}F). As outlined above, the relative intensities of the ^{19}F NMR resonances change over time. More precisely, the relative intensity of the resonance assigned to $Ti^{IV}_2\square$-F species decreases whereas the relative intensity of the resonance assigned to $Ti^{III}_2\square$-F, $Ti^{IV}_2Ti^{III}$-F, Ti^{IV}_2Al-F, $Ti^{IV}Al\square$-F and $Ti^{III}Al\square$-F species increases. Concomitantly, it has been shown that Al^{3+} ions move (migrate) from non-fluorinated $^{[4]}$Al and $^{[5]}$Al sites to $^{[6]}$Al sites and the changes over the time of the ^{19}F NMR spectra highlight the filling of vacancies of remaining $Ti^{IV}_2\square$-F species giving Ti^{IV}_2Al-F and then fluorinated $^{[6]}$Al site.

Density Functional Theory Calculations

Paired Ti-vacancy geometry-changes under sequential Al^{3+} intercalation

Figure S11 shows the changes in site-coordination geometry upon sequential Al^{3+} insertion from our DFT-optimised structural models. Before Al^{3+} insertion, the V_{Ti} sites approximate tetragonally distorted octahedra, with distances between equatorial anions of ~3.9 Å and between axial octahedra of ~4.6 Å. The first Al^{3+} ion insertion produces a strong contraction of the insertion site, which adopts a more regular octahedral coordination geometry with equatorial and axial anion–anion distances of 3.6 Å–3.7 Å. This local contraction is accompanied by an *expansion* of the adjacent vacant site: in particular, the anion–anion distance along the equatorial axis common to both sites increases from to ~3.85 Å to ~3.98 Å. This cooperative contraction of the intercalated site and expansion of the still-vacant site means the surrounding lattice is only moderately perturbed: the combined distance across both site changes from 7.71 Å to 7.61 Å. By inserting a second Al^{3+} ion this cooperative distortion of the two sites is disrupted. Both inserted Al^{3+} ions would ideally distort the surrounding structure into a regular octahedral coordination environment with contracted anion–anion distances. Doing so, however, would require an expansion of the adjacent site, which then destabilises the adjacent intercalated Al^{3+}. This has two effects, both of which contribute to double-Al^{3+} insertion being less favourable than single-Al^{3+} insertion. Firstly, neither Al^{3+} is able to achieve an “ideal” octahedral coordination environment. Instead both sites exhibit slight tetragonal distortion along the shared previously-equatorial axis. Secondly, the combined distance across both sites decreases to 7.46 Å, compared to ~7.62 Å in the singly-occupied model and to 7.71 Å in the initial double-vacancy model. This indicates additional strain imposed on the surrounding lattice, which contributes to double Al-insertion being energetically less favoured than single Al-insertion.

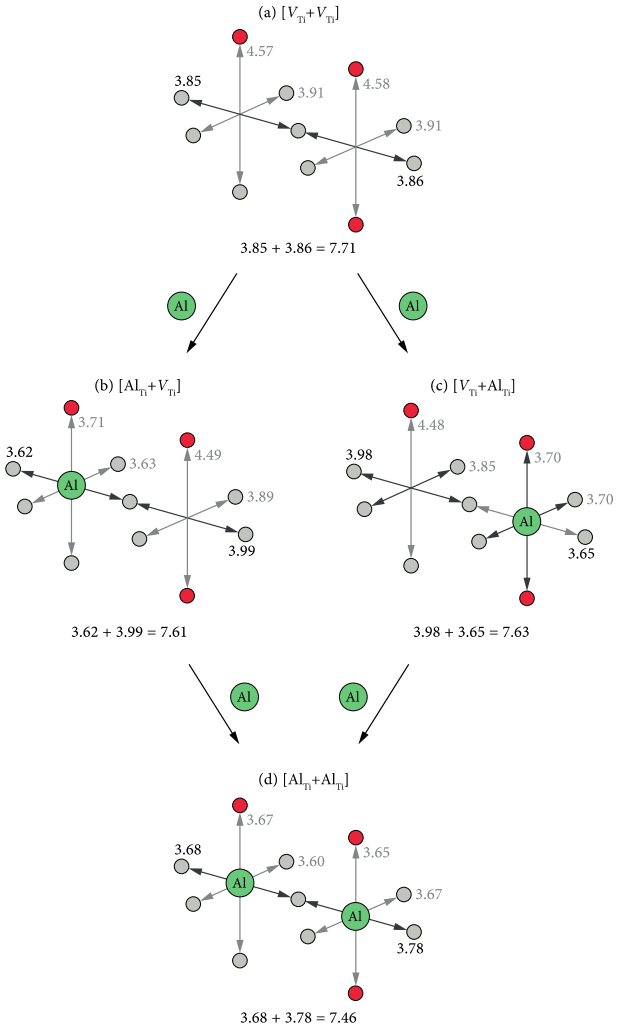

Figure S11. Schematic of the changes in geometry of the V_{Ti} octahedra in the [V_{Ti}+V_{Ti}] paired-vacancy model for sequential Al^{3+} insertion. All distances are given in Angstroms. The red and grey spheres refer to oxide and fluoride anions, respectively. The corresponding DFT-optimised structure files are available under the CC-BY-4.0 license as part of reference[24].

References

[1] W. Li, D. Corradini, M. Body, C. Legein, M. Salanne, J. Ma, K. W. Chapman, P. J. Chupas, A.-L. Rollet, C. Julien, K. Zhagib, M. Duttine, A. Demourgues, H. Groult, D. Dambournet, *Chem. Mater.* **2015**, *27*, 5014–5019.
[2] A. P. Hammersley, S. O. Svensson, M. Hanfland, A. N. Fitch, D. Hausermann, *High Pressure Research* **1996**, *14*, 235–248.
[3] X. Qiu, J. W. Thompson, S. J. L. Billinge, *Journal of Applied Crystallography* **2004**, *37*, 678–678.
[4] C. L. Farrow, P. Juhas, J. W. Liu, D. Bryndin, E. S. Božin, J. Bloch, T. Proffen, S. J. L. Billinge, *Journal of Physics: Condensed Matter* **2007**, *19*, 335219.
[5] E. Nimerovsky, R. Gupta, J. Yehl, M. Li, T. Polenova, A. Goldbourt, *Journal of Magnetic Resonance* **2014**, *244*, 107–113.
[6] S. Cavadini, A. Lupulescu, S. Antonijevic, G. Bodenhausen, *J. Am. Chem. Soc.* **2006**, *128*, 7706–7707.
[7] E. Lippmaa, A. Samoson, M. Magi, *Journal of the American Chemical Society* **1986**, *108*, 1730–1735.
[8] A. Medek, J. S. Harwood, L. Frydman, *Journal of the American Chemical Society* **1995**, *117*, 12779–12787.
[9] J.-P. Amoureux, C. Fernandez, S. Steuernagel, *Journal of Magnetic Resonance, Series A* **1996**, *123*, 116–118.
[10] D. Massiot, *Journal of Magnetic Resonance, Series A* **1996**, *122*, 240–244.
[11] D. Massiot, F. Fayon, M. Capron, I. King, S. Le Calvé, B. Alonso, J.-O. Durand, B. Bujoli, Z. Gan, G. Hoatson, *Magnetic Resonance in Chemistry* **2002**, *40*, 70–76.
[12] G. Kresse, J. Hafner, *J. Phys.: Condens. Matter* **1994**, *6*, 8245.
[13] G. Kresse, J. Furthmüller, *Computational Materials Science* **1996**, *6*, 15–50.
[14] G. Kresse, D. Joubert, *Phys. Rev. B* **1999**, *59*, 1758–1775.
[15] J. P. Perdew, A. Ruzsinszky, G. I. Csonka, O. A. Vydrov, G. E. Scuseria, L. A. Constantin, X. Zhou, K. Burke, *Phys. Rev. Lett.* **2008**, *100*, 136406.
[16] S. L. Dudarev, A. I. Liechtenstein, M. R. Castell, G. A. D. Briggs, A. P. Sutton, *Phys. Rev. B* **1997**, *56*, 4900–4908.
[17] S. L. Dudarev, G. A. Botton, S. Y. Savrasov, C. J. Humphreys, A. P. Sutton, *Phys. Rev. B* **1998**, *57*, 1505–1509.
[18] T. Koketsu, J. Ma, B. J. Morgan, M. Body, C. Legein, W. Dachraoui, M. Giannini, A. Demortière, M. Salanne, F. Dardoize, H. Groult, O. J. Borkiewicz, K. W. Chapman, P. Strasser, D. Dambournet, *Nature Materials* **2017**, *16*, 1142–1148.
[19] B. J. Morgan, G. W. Watson, *J. Phys. Chem. Lett.* **2011**, *2*, 1657–1661.
[20] B. J. Morgan, G. W. Watson, *Phys. Rev. B* **2010**, *82*, 144119.
[21] B. J. Morgan, P. A. Madden, *Phys. Rev. B* **2012**, *86*, 035147.
[22] J. Ma, T. Koketsu, B. J. Morgan, C. Legein, M. Body, P. Strasser, D. Dambournet, *Chem. Commun.* **2018**, *54*, 10080–10083.
[23] J. Ma, W. Li, B. J. Morgan, J. Światowska, R. Baddour-Hadjean, M. Body, C. Legein, O. J. Borkiewicz, S. Leclerc, H. Groult, F. Lantelme, C. Laberty-Robert, D. Dambournet, *Chem. Mater.* **2018**, *30*, 3078–3089.

[24] B. Morgan, **Computational Supporting Dataset: Atomic Insights into Aluminium-Ion Insertion in Defective Hydroxyfluorinated Anatase for Batteries.Bath: University of Bath Research Data Archive. doi.org/10.15125/BATH-00815**.
[25] T. E. Oliphant, *Guide to NumPy*, CreateSpace Independent Publishing Platform, USA, **2015**.
[26] S. van der Walt, S. C. Colbert, G. Varoquaux, *Computing in Science Engineering* **2011**, *13*, 22–30.
[27] S. P. Ong, W. D. Richards, A. Jain, G. Hautier, M. Kocher, S. Cholia, D. Gunter, V. L. Chevrier, K. A. Persson, G. Ceder, *Computational Materials Science* **2013**, *68*, 314–319.
[28] J. Köster, S. Rahmann, *Bioinformatics* **2012**, *28*, 2520–2522.
[29] B. J. Morgan, *Vasppy*, Zenodo, **2019**.
[30] R. Hoppe, St. Becker, *Zeitschrift für anorganische und allgemeine Chemie* **1989**, *568*, 126–135.
[31] P. Daniel, A. Bulou, M. Rousseau, J. Nouet, M. Leblanc, *Physical Review B* **1990**, *42*, 10545–10552.
[32] A. Le Bail, C. Jacoboni, M. Leblanc, R. De Pape, H. Duroy, J. L. Fourquet, *Journal of Solid State Chemistry* **1988**, *77*, 96–101.
[33] N. Herron, D. L. Thorn, R. L. Harlow, G. A. Jones, J. B. Parise, J. A. Fernandez-Baca, T. Vogt, *Chemistry of Materials* **1995**, *7*, 75–83.
[34] A. Sadoc, M. Biswal, M. Body, C. Legein, F. Boucher, D. Massiot, F. Fayon, *Solid State Nuclear Magnetic Resonance* **2014**, *59–60*, 1–7.